

COLLISIONAL FRAGMENTATION IS NOT A BARRIER TO CLOSE-IN PLANET FORMATION

JOSHUA WALLACE^{1,*}, SCOTT TREMAINE^{2,1}, AND JOHN CHAMBERS³

¹ Department of Astrophysical Sciences, Princeton University, Princeton, NJ 08544, USA

² Institute for Advanced Study, Princeton, NJ 08540, USA

³ Department of Terrestrial Magnetism, Carnegie Institution for Science, Washington, DC 20015, USA

Draft version March 7, 2024

ABSTRACT

Collisional fragmentation is shown to not be a barrier to rocky planet formation at small distances from the host star. Simple analytic arguments demonstrate that rocky planet formation via collisions of homogeneous gravity-dominated bodies is possible down to distances of order the Roche radius (r_{Roche}). Extensive N-body simulations with initial bodies $\gtrsim 1700$ km that include plausible models for fragmentation and merging of gravity-dominated bodies confirm this conclusion and demonstrate that rocky planet formation is possible down to $\sim 1.1 r_{\text{Roche}}$. At smaller distances, tidal effects cause collisions to be too fragmenting to allow mass build-up to a final, dynamically stable planetary system. We argue that even differentiated bodies can accumulate to form planets at distances that are not much larger than r_{Roche} .

Subject headings: planets and satellites: formation—planets and satellites: dynamical evolution and stability—planet–star interactions

1. INTRODUCTION

Exoplanetary systems possess a large and surprising diversity of architectures. In particular, many systems contain one or more planets with periods $\lesssim 10$ days. A partial list of examples includes Kepler-42, a $\sim 0.13 M_{\odot}$ star with three known planets, all rocky, with periods ~ 0.5 , ~ 1.2 , ~ 1.9 days (Muirhead et al. 2012); Kepler-32, a $\sim 0.58 M_{\odot}$ star with five known planets, having periods between ~ 0.7 and ~ 22 days (Muirhead et al. 2012); and TRAPPIST-1, a $\sim 0.08 M_{\odot}$ star with seven known planets, all with radii $\sim 1 R_{\oplus}$ and periods between ~ 1.5 and ~ 19 days (Gillon et al. 2017).

A central question is whether (i) such close-in planetary systems can form *in situ*, or (ii) they formed further out from their host star and migrated inwards to their current configuration. There are difficulties with both mechanisms. (i) Assuming solar metallicity, the gas surface density of a disk containing sufficient metals for *in situ* formation of close-in planets such as those highlighted above would be gravitationally unstable (Raymond & Cossou 2014; Schlichting 2014). Such disks should therefore form giant rather than small rocky planets. Moreover, even if the disk were stable, the high temperatures (~ 2000 K) expected in the inner disk would prevent the condensation of dust within 0.1 AU (D’Alessio et al. 1998). A possible solution is that inward migration of solid material through the protoplanetary disk could allow for sufficient planet-building material to accrue at small semi-major axes without an unstable build up of gas (e.g., Youdin & Shu 2002; Youdin & Chiang 2004; Chiang & Youdin 2010; Chatterjee & Tan 2014, 2015). (ii) Although the physics of planet migration is robust, the behavior of migrating planets depends sensitively on the properties and physics of protoplanetary disks (e.g., Baruteau et al. 2014). Simple models of migration incorrectly predict that most short-period plan-

ets should be in orbital resonances, and cannot explain the large numbers of short-period planets discovered by the *Kepler* spacecraft (e.g., Benz et al. 2014).

In this paper, we examine another possible barrier to *in situ* formation of close-in planets: collisional fragmentation. Even if planetesimals or planetary embryos can form at or migrate to these short-period orbits, would the relative velocities between such bodies allow for merging and growth, or would they be sufficiently large that collisions would be primarily fragmenting? In the latter case, planetesimals would not be able to grow into planets. We address this question both analytically and with N-body simulations.

The destruction of bodies due to collisions has been studied in depth in the context of asteroids, the Kuiper belt, and debris disks (e.g., Dohnanyi 1969; Wyatt & Dent 2002; Dominik & Decin 2003; Kobayashi & Tanaka 2010; Kenyon & Bromley 2017b; Pan & Sari 2005). However, the bodies focused on in these studies are $\lesssim 100$ km in size (and many are $\lesssim 1$ km), much smaller than the bodies that will be examined in this work. The physics of fragmentation is different in small and large bodies, with small bodies ($\lesssim 0.1$ – 1 km for rocky bodies) being held together primarily by their internal strength (and thus affected by internal flaws and cracks) and large bodies being held together primarily by their gravitational self-attraction (although many small bodies are actually rubble piles with little internal strength; we note Pan & Sari 2005 assumed this in their collision models). The results of a fragmenting collision also depend on body size: larger bodies have significant escape velocities and thus some of the fragments from an impact can be reaccreted. Collision velocities between large bodies, especially late in the planet-formation process when they are on well-separated and nearly stable orbits, can also differ from those of small bodies, which have random velocities that are themselves often set by stirring from the large bodies. In particular, the models of debris-disk pro-

*joshua.jw@princeton.edu

duction via collisional cascades are generally based on a bimodal mass distribution with the largest bodies having undergone runaway growth and stirring up the smaller bodies to sufficiently high random velocities to have destructive collisions. In this picture, the larger remnants from runaway growth are what eventually form the final planets and are the focus of the present study. For these reasons, results from collisional cascade models of small bodies cannot be assumed to carry over to the large bodies that eventually form planets.

In Section 2 we provide an analytic motivation for our study, then in Section 3 we describe the methods of our N-body simulations. We present the results from the simulations in Section 4, provide a discussion in Section 5, and conclude in Section 6.

2. ANALYTIC MOTIVATION

2.1. Preliminaries

Here we present an order-of-magnitude argument describing the necessary conditions for collisions between gravity-dominated bodies to be erosive. We define “erosive” to mean that the largest remnant after a collision is less massive than the larger of the two colliding bodies. Throughout this work, we always assume that the colliding bodies have sufficient mass that their gravitational binding energy is greater than their molecular binding energy (the gravity-dominated regime). We also assume that collisions are between two spherical bodies of the same density, having masses m_1 and m_2 and radii R_1 and R_2 . We specify $m_1 \geq m_2$ and, following common convention, call the larger body involved in the collision the “target” and the smaller body the “projectile”. In this section, we assume all orbits are coplanar (no mutual inclination).

The amount of fragmentation that occurs in a collision depends on the ratio between the specific impact energy in the center-of-mass frame Q and some threshold energy Q^* , defined to be the specific impact energy necessary to disperse half the mass involved in the collision. The impact energy is

$$Q = \frac{\mu(\Delta v)^2}{2(m_1 + m_2)}, \quad (1)$$

where μ is the reduced mass of the two colliding bodies and Δv their collision velocity (the relative velocity just before impact). From, e.g., Stewart & Leinhardt (2012)

$$Q^* = \left(\frac{\mu}{\mu_\beta}\right)^{3/2} \left[\frac{(1+\alpha)^2}{4\alpha}\right] \frac{4}{5} C^* \pi \rho_1 G R_{C1}^2, \quad (2)$$

where μ_β is the reduced mass of the target body and the fraction β of the projectile body that intersects the target body during a collision, which for off-center collisions may be less than unity (see Stewart & Leinhardt 2012 for details), $\alpha = m_2/m_1$, C^* is a dimensionless factor that accounts for the dissipation of energy in the target body, $\rho_1 = 1 \text{ g cm}^{-3}$, G is the gravitational constant, and R_{C1} is the radius of a body with density ρ_1 and a mass equal to the sum of the projectile and target masses,

$$\frac{4\pi\rho_1}{3} R_{C1}^3 = m_1 + m_2. \quad (3)$$

Leinhardt & Stewart (2012) (hereafter LS12) found the

best-fit value of C^* for planet-sized bodies is 1.9 ± 0.3 ; Chambers (2013) (hereafter C13) used $C^* = 1.8$ and we use that value in this work. Note that the expressions of Equation (2) in Stewart & Leinhardt (2012) (primarily their equation 10) are more general because they contain an extra parameter, the velocity exponent $\bar{\mu}$. Following C13 and consistent with the best-fit values found by Stewart & Leinhardt (2012), we use $\bar{\mu} = 1/3$ to get Equation (2).

In this section, we assume that collisions are between bodies on initially well-separated, near-circular orbits whose eccentricities have been gradually excited by mutual perturbations. This situation arises, for example, in the late stages of planet formation after oligarchic growth is complete and the population of residual small bodies has decayed. (This is in contrast to the early stages of planet formation, where there is a much higher density of colliding bodies and the random velocities are set by the escape velocity of the largest bodies.) If the two bodies initially have semi-major axes $a \pm \Delta a/2$, with $\Delta a \ll a$, then their relative speed $(\Delta v)_{\text{rel}}$ —when they are close to colliding but far enough away that gravitational focusing is unimportant—will be

$$(\Delta v)_{\text{rel}} = f_1 \left(\frac{GM_*}{a}\right)^{1/2} \frac{\Delta a}{a} = f_1 v_c \frac{\Delta a}{a}, \quad (4)$$

where M_* is the mass of the central star, $v_c = \sqrt{GM_*/a}$ is the Keplerian circular velocity at a , and f_1 is a factor of order unity. Two such bodies are unable to collide unless the eccentricity $e \gtrsim \Delta a/a$. Including gravitational focusing, the collision velocity Δv between these two bodies will be

$$\Delta v = [(\Delta v)_{\text{rel}}^2 + v_e^2]^{1/2}, \quad (5)$$

where v_e is the mutual escape velocity, which we define as

$$v_e = \sqrt{2G \frac{m_1 + m_2}{R_1 + R_2}}. \quad (6)$$

2.2. Equal-mass Case

Assuming the bodies have the same mass m and density ρ (and thus the same radius R) and have a head-on collision so $\mu = \mu_\beta$, the specific impact energy scaled by Q^* is

$$\frac{Q}{Q^*} = \frac{\mu}{2(m_1 + m_2)} \frac{(\Delta v)^2}{Q^*} \quad (7)$$

$$= \frac{1}{8} \frac{(\Delta v)_{\text{rel}}^2 + v_e^2}{Q^*} \quad (8)$$

$$\simeq \frac{1}{8} \left[\frac{5f_1^2 M_* (\Delta a)^2}{4\pi\rho_1 C^* a^3 R_{C1}^2} + \frac{v_e^2}{Q^*} \right] \quad (9)$$

$$= \frac{1}{8} \left[\frac{5f_1^2 M_* (\Delta a)^2}{2^{4/3} 3^{2/3} \pi^{1/3} \rho_1^{1/3} C^* a^3 m^{2/3}} + \frac{v_e^2}{Q^*} \right]. \quad (10)$$

The quantity v_e^2/Q^* can be simplified as follows. First,

$$\frac{v_e^2}{Q^*} = \frac{5(m_1 + m_2)}{2\pi\rho_1 C^* (R_1 + R_2) R_{C1}^2}. \quad (11)$$

Eliminating ρ_1 using Equation (3), we get

$$\frac{v_e^2}{Q^*} = \frac{10R_{C1}}{3C^*(R_1 + R_2)}. \quad (12)$$

For arbitrary masses,

$$R_{C1} = \left[\frac{3(m_1 + m_2)}{4\pi\rho_1} \right]^{1/3}, \quad (13)$$

$$R_1 + R_2 = \left(\frac{3}{4\pi\rho} \right)^{1/3} (m_1^{1/3} + m_2^{1/3}). \quad (14)$$

Hence, for equal-mass bodies,

$$\frac{Q}{Q^*} \simeq \frac{5f_1^2 M_* (\Delta a)^2}{2^{13/3} 3^{2/3} \pi^{1/3} \rho_1^{1/3} C^* a^3 m^{2/3}} + \frac{5}{3C^* 2^{8/3}} \left(\frac{\rho}{\rho_1} \right)^{1/3}. \quad (15)$$

Equation (15) can be rewritten in terms of the mutual Hill radius, $r_{\text{Hill}} = a[(m_1 + m_2)/(3M_*)]^{1/3}$,

$$\frac{Q}{Q^*} \simeq \frac{5f_1^2}{2^{11/3} 3^{4/3} \pi^{1/3} C^*} \left(\frac{M_*}{\rho_1 a^3} \right)^{1/3} \frac{(\Delta a)^2}{r_{\text{Hill}}^2} + \frac{5}{3C^* 2^{8/3}} \left(\frac{\rho}{\rho_1} \right)^{1/3}. \quad (16)$$

The criterion that head-on collisions of equal-mass bodies are non-erosive is $Q < Q^*$. For later use we shall write this as $Q < f_2 Q^*$ with $f_2 = 1$ for equal-mass bodies. Thus we obtain a necessary condition for accumulation,

$$\frac{5f_1^2}{2^{11/3} 3^{4/3} \pi^{1/3} C^*} \left(\frac{M_*}{\rho_1 a^3} \right)^{1/3} \frac{(\Delta a)^2}{r_{\text{Hill}}^2} \lesssim f_2 - \frac{5}{3C^* 2^{8/3}} \left(\frac{\rho}{\rho_1} \right)^{1/3}. \quad (17)$$

Equation (17) sets a maximum value for the initial separation Δa at which two colliding bodies avoid an erosive collision. For future use, we note that the relation between f_2 and the minimum collision velocity for erosive head-on collisions between equal-mass bodies can be written

$$\frac{(\Delta v)^2}{v_e^2} = \frac{3 \cdot 2^{8/3}}{5} f_2 C^* \left(\frac{\rho_1}{\rho} \right)^{1/3}. \quad (18)$$

If the typical separation in the post-collision system (which we call $\Delta a'$) is too small, then the system will be dynamically unstable and eventually undergo another collision. An approximate stability criterion is $\Delta a' \gtrsim f_3 r_{\text{Hill}}$, where $f_3 \simeq 10$ for stability over 10^{10} orbits (Pu & Wu 2015) and the primes are used to distinguish post-collision properties from pre-collision properties. We note the chaotic nature of collisional growth, but still choose to employ this criterion as it is a necessary one for stability in the long-lived post-collision stage, not the short-lived chaotic collision stage. This gives us a lower bound on dynamically stable $\Delta a'$, while Equation (17) gives us an upper bound on Δa for collisions to be non-erosive. If we assume a system of bodies with equal masses m , separated from their nearest

companions in semi-major axis by Δa just prior to their last collision before stability, and if we also assume that adjacent bodies collide and merge pairwise (this ignores the possibility of higher-eccentricity collisions between non-adjacent bodies), then the post-collision bodies will be separated from each other by $\Delta a' \simeq 2\Delta a$ and will have $r'_{\text{Hill}} \simeq 2^{1/3} r_{\text{Hill}}$. Thus, the post-collision stability condition $\Delta a' \gtrsim f_3 r'_{\text{Hill}}$ can be rewritten in terms of pre-collision quantities, $2^{2/3} \Delta a \gtrsim f_3 r_{\text{Hill}}$. Plugging this into Equation (17) to eliminate Δa , we obtain a range for a in which collisions will not be erosive up to the final collision before long-term dynamical stability,

$$a \gtrsim \frac{5f_1^2 f_3^2}{32\pi^{1/3} 3^{4/3} C^*} \left(\frac{M_*}{\rho_1} \right)^{1/3} \times \left[f_2 - \frac{5}{3C^* 2^{8/3}} \left(\frac{\rho}{\rho_1} \right)^{1/3} \right]^{-1}. \quad (19)$$

Remarkably, this criterion is independent of the planetesimal mass m .

The Roche radius r_{Roche} for a homogeneous body of density ρ is

$$r_{\text{Roche}} = 1.523 \left(\frac{M_*}{\rho} \right)^{1/3} = 0.0089 \text{ AU} \left(\frac{M_*}{M_\odot} \frac{3 \text{ g cm}^{-3}}{\rho} \right)^{1/3}. \quad (20)$$

If a gravity-dominated body on a circular orbit has $a < r_{\text{Roche}}$, it is disrupted by tidal forces. Writing Equation (19) in terms of r_{Roche} and using $C^* = 1.8$, we get

$$a \gtrsim \frac{5f_1^2 f_3^2}{32\pi^{1/3} 3^{4/3} C^*} \left(\frac{\rho}{\rho_1} \right)^{1/3} \frac{r_{\text{Roche}}}{1.523} \times \left[f_2 - \frac{5}{3C^* 2^{8/3}} \left(\frac{\rho}{\rho_1} \right)^{1/3} \right]^{-1} \gtrsim 0.013 \frac{f_1^2 f_3^2 \eta^{1/3}}{f_2 - 0.21\eta^{1/3}} r_{\text{Roche}}, \quad (21)$$

where $\eta = \rho/3 \text{ g cm}^{-3}$ and $\rho/\rho_1 = 3\eta$. This is the semi-major axis range in which the last collisions before long-term dynamical stability will not be erosive. Apart from the dimensionless factors f_1, f_2, f_3 , the value of a at which a system transitions from non-erosive to erosive collisions is less than r_{Roche} .¹ Since gravity-dominated bodies cannot survive within r_{Roche} , to decide whether collisional fragmentation is an additional barrier to growth we must determine whether the transition point is inside or outside r_{Roche} .

We now determine reasonable values for f_1, f_2 , and f_3 . As noted previously, Pu & Wu (2015) found that $f_3 \simeq 10$. A linear expansion in a of orbital velocity v around v_c gives $f_1 \simeq 0.5$. As mentioned earlier, for equal-mass bodies, $f_2 = 1$. If we scale f_1, f_2 , and f_3 by these

¹ One caveat is that we do not consider the effects of the strong tides present near r_{Roche} , which may reduce Q^* . The effect of tides is discussed further in Section 3.1.

values, then from Equation (21) we find

$$a \gtrsim a_{\text{frag}} = 0.41 r_{\text{Roche}} \times \left(\frac{f_1}{0.5}\right)^2 \left(\frac{f_3}{10}\right)^2 \eta^{1/3} \frac{1 - 0.21}{f_2 - 0.21\eta^{1/3}} \quad (22)$$

$$= 0.0036 \text{ AU} \left(\frac{M_*}{M_\odot}\right)^{1/3} \times \left(\frac{f_1}{0.5}\right)^2 \left(\frac{f_3}{10}\right)^2 \frac{1 - 0.21}{f_2 - 0.21\eta^{1/3}}, \quad (23)$$

where a_{frag} is the semi-major axis at which collisions between equal-mass bodies transition from non-erosive to erosive. For comparison, the solar radius is 0.0047 AU. For these values of f_1 , f_2 , and f_3 , the semi-major axis range in which collisions are primarily erosive will *always* be less than r_{Roche} , i.e., the bodies will be tidally disrupted before they are close enough to their host star to reach high enough collision velocities to erode one another. If we have chosen correct values for f_1 , f_2 , and f_3 , then Equation (22) says that gravity-dominated bodies, once formed, are able to engage in non-erosive collisions for semi-major axes all the way down to r_{Roche} , independent of stellar mass and the mass and density of the bodies. However, modifications to f_1 , f_2 , and f_3 could lead to erosive collisions outside r_{Roche} . We give two brief examples:

- Kenyon & Bromley (2017b) model collisional cascades in strength-dominated bodies and find that $(\Delta v)^2/Q^* \geq 5$ led to erosion of the largest bodies. Equation (1) implies that $Q < (\Delta v)^2/8$ for the largest body in a continuous mass distribution, so this would mean that $f_2 \lesssim 0.6$. A value $f_2 = 0.6$, with the fiducial parameters in Equation (22), leads to $a_{\text{frag}} = 0.83 r_{\text{Roche}}$.
- Our results only hold for homogeneous bodies. Using hydrodynamical simulations of collisions between differentiated bodies, Asphaug (2010) found that equal-mass head-on collisions were non-erosive if $\Delta v < kv_e$ and $k \simeq 2.9$. For our fiducial parameters $C^* = 1.8$ and $\rho/\rho_1 = 3$, Equation (18) implies that $k^2 = 4.75f_2$, so this value of k implies $f_2 = 1.8$. However, Asphaug also found that the crusts and mantles of differentiated bodies are more easily stripped in collisions (particularly off-center collisions) than the outer parts of homogeneous bodies. His simulations show that collisions with an angle θ between the relative velocity vector and relative center-of-mass vector $\sim 30^\circ$ have $k \approx 1.5$ ($f_2 = 0.5$ for our fiducial parameters) and collisions with $\theta \gtrsim 45^\circ$ have even lower values, $k \approx 1.2$ – 1.4 ($f_2 = 0.3$ – 0.4). If $f_2 = 0.3$ – 0.4 and f_1 , f_3 , and η respectively remain 0.5, 10, and 1, then from Equation (22), $a_{\text{frag}}/r_{\text{Roche}} = 3.6$ – 1.7 . However, the fractional mass loss in these off-center collisions remains quite low over a large range of k . For $\theta = 30^\circ$ the fractional mass loss is $\lesssim 5\%$ for $k \lesssim 1.7$ ($f_2 \simeq 0.61$), which occurs for $a > 0.81 r_{\text{Roche}}$. Additionally, the mass loss for a given k decreases with increasing θ . Equal-mass collisions

with $\theta = 45^\circ$ have $\lesssim 5\%$ fractional mass loss for $k \lesssim 2.2$ ($f_2 \simeq 1.1$), and $\theta = 60^\circ$ gives $\sim 2\%$ fractional mass loss even for $k = 3$ ($f_2 = 1.9$). The shallow slope of mass loss versus collision velocity for off-center collisions is balanced by the mass growth from low-velocity off-center and low- and high-velocity head-on collisions. These arguments suggest that our conclusion for homogeneous equal-mass bodies, that collisional fragmentation is not a barrier to planet formation all the way down to r_{Roche} , likely holds for differentiated bodies as well.

2.3. Unequal-mass Case

The preceding arguments can be generalized to bodies with unequal masses, though not quite as cleanly. Assuming that the collision is sufficiently close to head-on that $\mu = \mu_\beta$ (and with $m_1 \geq m_2$ and $\alpha = m_2/m_1$ as before), we can write a more general form of Equation (10),

$$\frac{Q}{Q^*} = \frac{\mu}{2(m_1 + m_2)} \frac{(\Delta v)_{\text{rel}}^2 + v_e^2}{Q^*} \quad (24)$$

$$= \frac{\alpha}{2(1 + \alpha)^2} \left[\frac{5\alpha f_1^2 M_* (\Delta a)^2}{(1 + \alpha)^2 \pi \rho_1 C^* a^3 R_{C1}^2} + \frac{v_e^2}{Q^*} \right] \quad (25)$$

$$= \frac{\alpha}{2(1 + \alpha)^2} \times \left[\frac{5 \cdot 2^{4/3} \alpha f_1^2 M_* (\Delta a)^2}{3^{2/3} (1 + \alpha)^{8/3} \pi^{1/3} \rho_1^{1/3} C^* a^3 m_1^{2/3}} + \frac{v_e^2}{Q^*} \right]. \quad (26)$$

Still assuming that both bodies have the same density, we may follow steps similar to those in Equations (11)–(15) to obtain

$$\frac{Q}{Q^*} = \frac{\alpha}{2(1 + \alpha)^2} \left[\frac{5 \cdot 2^{4/3} \alpha f_1^2 M_* (\Delta a)^2}{3^{2/3} (1 + \alpha)^{8/3} \pi^{1/3} \rho_1^{1/3} C^* a^3 m_1^{2/3}} + \frac{40}{3C^*} \frac{\alpha}{(1 + \alpha)^{5/3} (1 + \alpha^{1/3})} \left(\frac{\rho}{\rho_1}\right)^{1/3} \right]. \quad (27)$$

We substitute r_{Hill} as defined after Equation (15), now expressed in terms of m_1 and α , into Equation (27) and obtain more general versions of Equation (16),

$$\frac{Q}{Q^*} = \frac{\alpha^2}{(1 + \alpha)^4} \times \left[\frac{5 \cdot 2^{1/3} f_1^2}{3^{4/3} \pi^{1/3} C^*} \left(\frac{M_*}{\rho_1 a^3}\right)^{1/3} \frac{(\Delta a)^2}{r_{\text{Hill}}^2} + \frac{20}{3C^*} \frac{(1 + \alpha)^{1/3}}{1 + \alpha^{1/3}} \left(\frac{\rho}{\rho_1}\right)^{1/3} \right], \quad (28)$$

and Equation (17),

$$\frac{(1 + \alpha)^4}{\alpha^2} f_2 - \frac{20}{3C^*} \frac{(1 + \alpha)^{1/3}}{1 + \alpha^{1/3}} \left(\frac{\rho}{\rho_1}\right)^{1/3} \gtrsim \frac{5 \cdot 2^{1/3} f_1^2}{3^{4/3} \pi^{1/3} C^*} \left(\frac{M_*}{\rho_1 a^3}\right)^{1/3} \frac{(\Delta a)^2}{r_{\text{Hill}}^2}. \quad (29)$$

We use similar arguments as before regarding the pre- and post-collision values for Δa and r_{Hill} , except that we relax the assumption that the masses of the bodies

are all the same. As before, $\Delta a' \simeq 2\Delta a$. However, the post-collision mutual Hill radius r'_{Hill} depends not only on the mass of the newly merged body but also the masses of the nearest neighbors, which, in principle, could take any value. Using c to express the mass ratio between the newly merged body (of mass m_1+m_2) and the mass m_3 of a nearby body of interest, $m_3 = c(m_1+m_2)$, we can write $r'_{\text{Hill}} \simeq (1+c)^{1/3} r_{\text{Hill}}$. Thus, the condition $\Delta a' \gtrsim f_3 r'_{\text{Hill}}$ becomes $2\Delta a \gtrsim (1+c)^{1/3} f_3 r_{\text{Hill}}$. From this, we obtain an analog to Equation (19) in the case of arbitrary masses,

$$a \gtrsim \frac{5f_1^2 f_3^2 (1+c)^{2/3}}{2^{5/3} 3^{4/3} \pi^{1/3} C^*} \left(\frac{M_*}{\rho_1} \right)^{1/3} \times \left[\frac{(1+\alpha)^4}{\alpha^2} f_2 - \frac{20}{3C^*} \frac{(1+\alpha)^{1/3}}{1+\alpha^{1/3}} \left(\frac{\rho}{\rho_1} \right)^{1/3} \right]^{-1}. \quad (30)$$

Expressing the result in units of r_{Roche} , we find

$$a \gtrsim \frac{5f_1^2 f_3^2 (1+c)^{2/3} \eta^{1/3}}{2^{5/3} 3^{4/3} \pi^{1/3} C^*} \frac{r_{\text{Roche}}}{1.523} \times \left[\frac{(1+\alpha)^4}{\alpha^2} f_2 - \frac{20\eta^{1/3}}{3^{2/3} C^*} \frac{(1+\alpha)^{1/3}}{1+\alpha^{1/3}} \right]^{-1}. \quad (31)$$

We now find the value of α that maximizes the right side of Equation (31). The parameter f_2 is a function of α (see the first line of Equation 8 in C13) and is expressed as such in our maximization. The value of α that maximizes Equation (31), as well as the maximum value, depend on the values of the various parameters in Equation (31). The factor f_1 does not depend on the masses of the bodies, and thus will keep its same value. We note that most of the work on orbital stability has focused on equal-mass bodies, so it is not known whether f_3 depends on relative masses²; we assume f_3 does not depend on mass. Thus, for the maximization, we assume as before $f_1 = 0.5$, $f_3 = 10$, $\eta = 1$, and $C^* = 1.8$, and we also assume $c = 1$. Since we have assumed $m_1 \geq m_2$, α must be in the interval $(0, 1]$. The local maximum in this domain using the assumed values of the other parameters is found at $\alpha = 0.49$ and gives

$$a \gtrsim a_{\text{frag},\alpha} = 0.51 r_{\text{Roche}}, \quad (32)$$

where $a_{\text{frag},\alpha}$ is the same as a_{frag} but generalized to arbitrary α . Thus our conclusions from the homogeneous equal-mass case should remain approximately valid for arbitrary mass ratios. For differentiated bodies, the arguments presented before based on the results of Asphaug (2010) still hold, as for head-on collisions, $f_2 \simeq 1.3$ for $\alpha = 0.5$ and $f_2 \simeq 1.5$ for $\alpha = 0.1$ (which are the only two unequal mass ratios examined in Asphaug 2010), and for off-center collisions, all f_2 values are greater for $\alpha = 0.5, 0.1$ collisions than the $\alpha = 1$ collisions with corresponding θ .

Our statement that collisions lead to growth if $Q < f_2 Q^*$ ignores any dependence of f_2 on stellar tides. Close to r_{Roche} , tides from the star will make it easier for fragments to escape the gravitational influence of whatever

² The dependence on the relative mass is likely to be weak, since Hill's equations describing the interactions of two small bodies orbiting a much larger third body depend only on the sum of the masses of the two small bodies (e.g., Hénon & Petit 1986).

coalesced body may be left after a collision, and thus f_2 will take a smaller value than at larger semi-major axes. This is accounted for in our numerical work by modifying the escape speed, as described in Section 3.1. An additional complication not addressed by our analytic work is that collisions will take on a variety of impact parameters and have different possible collision outcomes than the pure fragmentation outcome considered in this section. Because of these additional considerations, and because of the sensitivity of our analytic result to even small uncertainties in f_1 , f_2 , and f_3 , it is essential to perform N-body simulations of systems of rocky bodies to test the analytic results of this section. The remainder of this work presents the methods and results of such calculations.

3. NUMERICAL METHODS

Our approach is very similar to that of C13, who studied the effect of collisional fragmentation on the formation of rocky planets in a solar system context. Our simulations were carried out using the hybrid-symplectic integrator in the *Mercury* N-body integrator package (Chambers 1999), including the modifications introduced in C13 to describe collisional fragmentation. We first describe the collision algorithm and then discuss the initial conditions of our simulations.

3.1. Collision Algorithm

The prescription used for collision outcomes is that of LS12 as implemented in C13, with modifications described below to account for stellar tides. Here we briefly describe the possible outcomes of a collision and direct the reader to C13 for a full description of the algorithm. When a collision is identified, the relative velocity (including gravitational focusing) at the time of impact is calculated. If the impact velocity is less than a modified mutual escape velocity v'_e , then the two bodies merge. This modified mutual escape velocity takes into account the relatively small Hill spheres of the bodies at the small semi-major axes present in our simulations. Instead of fragments needing to escape to infinity to become unbound from the bodies, they need only escape to the edge of the Hill sphere. This is accounted for by defining v'_e as follows,

$$v_e'^2 = \max \left\{ v_e^2 \left(1 - \frac{R_t + R_p}{r_{\text{Hill}}} \right), 0 \right\}, \quad (33)$$

where R_t and R_p are the radii of the target and the projectile, v_e is the escape speed defined in Equation (6), and r_{Hill} is the mutual Hill radius defined after Equation (15). If the impact velocity is greater than v'_e , then fragmentation occurs, and the largest remnant mass is calculated as outlined in Equation (8) of C13.

The mass from the impacting bodies not included in the largest remnant is then divided into one or more equal-mass fragments, with masses as close as possible to but not below a minimum fragment mass (MFM) that is specified for each simulation. If the remaining mass is less than the specified MFM, then the collision is treated as a merger and the total mass is placed in a single body.

The details of how non-head-on collisions are handled can be found in C13 and LS12. High impact-parameter collisions have other possible outcomes in addition to the

merger–fragmentation scenario presented above for head-on collisions. These are:

- hit-and-run collisions, where the target remains intact and the projectile is disrupted, in some cases adding mass to the target;
- graze-and-merge collisions, where an initial off-center collision saps sufficient kinetic energy from the system for an eventual merger.

We use the boundary identified by Genda et al. (2012) between the hit-and-run and graze-and-merge regimes, replacing the escape velocity v_{esc} in their Equation (16) with our modified escape velocity v'_e to account for stellar tides.

As was mentioned before, The amount of mass in a collision that is dispersed by fragmentation, if any, depends on the ratio between Q (given by Equation 1) and Q^* (given by Equation 2). Stewart & Leinhardt (2009) found that, in the catastrophic disruption regime, the largest remnant mass (and thus the mass dispersed by fragmentation) is linear in this ratio. However, this simple relation appears not to hold in regions close to the Roche radius (e.g., Karjalainen 2007; Hyodo & Ohtsuki 2014; see also Kenyon & Bromley 2017a for an application to collisional cascades). Instead, the mass of the largest remnant depends on the shapes of the colliding bodies and the relative magnitudes of the azimuthal, radial, and vertical components of the impact velocity (for the radial velocity component in particular, the dependence is not monotonic on specific impact energy). Since this study is focused more on answering the question of whether Keplerian orbit-driven collision velocities are ever large enough to prevent planet formation and not on precisely how tidal effects affect collisional planet formation, we approximate the tidal effects by replacing Q^* with Q^*_{tidal} , defined as

$$Q^*_{\text{tidal}}(r) = \begin{cases} Q^* \left[1 - (r_{\text{Roche}}/r)^3 \right] & r > r_{\text{Roche}} \\ 0 & r \leq r_{\text{Roche}}, \end{cases} \quad (34)$$

where r is the distance between the central star and the center of mass of the colliding bodies. For $r > r_{\text{Roche}}$, we found that Equation (34) predicts collision energies required to nearly entirely disrupt bodies that are broadly consistent with the simulations of Hyodo & Ohtsuki (2014). Equation (34) also converges to the LS12 results far away from the Roche radius, a result also found by Hyodo & Ohtsuki (2014). In the case $Q^*_{\text{tidal}} = 0$, any collision will cause the bodies to fragment into as many fragments as possible, as limited by the MFM. Thus, collisions that occur inside r_{Roche} will lead to complete disruption of the colliding bodies. In our algorithm, disruption inside the Roche radius only occurs during a collision, i.e., if a body migrates in to $r < r_{\text{Roche}}$, it will not be disrupted unless it suffers a collision while inside r_{Roche} .

We also note that we are using the classical Roche radius, which was derived for a strengthless, co-rotating body on a circular orbit and that more general forms of the disruption radius have been developed (e.g., Holsapple & Michel 2006, 2008). However, the strengthless

model approximates collisional fragmentation well, since after a collision the fragments are no longer bound to each other by tensile forces, only gravity. For this reason, and for simplicity, we use the classical Roche radius in Equation (34) and throughout the paper. We believe that the qualitative picture our results paint is correct while quantitative details that depend on the Roche radius may well be inaccurate.

The choice of MFM for our collision algorithm represents a compromise between computational cost and realism: if the MFM is too large, a large fraction of fragmenting collisions will be erroneously classified as mergers; if the MFM is too small, then fragmentation will create so many fragments that the numerical calculations will slow to a crawl. To check that our results are not strongly dependent on the choice of MFM, each set of initial conditions was run with three different values of the MFM, as detailed in Section 3.2.

If multiple collisions involving the same body occur in the same time step, only one of the collisions (chosen at random) was considered to have happened. For a typical run, this situation happened at most a few times over the course of the run. Any bodies that pass inside the solar radius (~ 0.0047 AU) were assumed to merge with the central star. Over the course of a typical run, this happened only a few times. Virtually all such events involved bodies with small masses (very near the MFM), and the resulting total mass loss was at most a few percent of the total mass of the initial bodies.

3.2. Initial Conditions

We carried out several sets of N-body integrations. We first describe the initial conditions of our fiducial set of simulations then describe the variations we made to this fiducial set. All of our systems orbit a $1\text{-}M_{\odot}$ star and we assume a fixed density of 3 g cm^{-3} for all bodies, independent of mass. A time step of 6×10^{-3} days was used. For simplicity, we assume that the star has a radius of $1 R_{\odot}$, but note that the young stars in systems such as those we simulate may have considerably larger radii (e.g., calculations by Baraffe et al. 2015 show that a $1\text{-}M_{\odot}$ star with an age of 3 Myr has a radius of $1.7 R_{\odot}$). Our 15 fiducial simulations start with 150 equal-mass bodies of individual mass $0.02 M_{\oplus}$ (~ 1.6 times the mass of the Moon), corresponding to a radius of ~ 2100 km with the 3 g cm^{-3} density used in this work). This mass is roughly what is expected for bodies that form during the runaway growth phase of planet formation (e.g., Wetherill & Stewart 1989) and thus our initial conditions can be thought of as the beginning of the oligarchic growth or giant-impact stage of planet formation.

We ran our simulations assuming no gas was present, i.e., we assumed that the protoplanetary gas disk at these radii had entirely disappeared by the beginning of our simulations. Thus our initial conditions can be thought of as corresponding to planetesimals/planetary embryos that were prevented from evolving into orbit-crossing trajectories by eccentricity damping while the gas was present, or planetesimals/planetary embryos that underwent disk-driven migration and were frozen in semi-major axis as the disk evaporated away. We caution that this assumption may not be realistic in some or perhaps all disks. The existence of planets like GJ 1214 b (Charbonneau et al. 2009)—a $\sim 7 M_{\oplus}$ planet at a period of 1.58

days that is believed to have a substantial gas envelope—implies that in at least some cases the formation of planets with ~ 1 -day orbital periods has occurred before the gas has completely disappeared.

The initial semi-major axes of the bodies were distributed between 0.005 and 0.04 AU using a similar disk surface-density profile $\sigma(a)$ as Chambers (2001) and C13: $\sigma \propto a^{-3/2}$ from 0.02 AU to 0.04 AU and, inside 0.02 AU, σ linear in a , starting from $\sigma = 0$ at 0.005 AU and increasing to a value matching the $a^{-3/2}$ profile at 0.02 AU. A cumulative distribution function was calculated from this disk profile and its inverse was sampled in 150 equally spaced locations to determine the initial semi-major axes of the bodies. This semi-major axis range was chosen to straddle the Roche radius (0.0089 AU for a $1\text{-}M_{\odot}$ star with planet density $\rho = 3\text{ g cm}^{-3}$), with the lower bound chosen to be close to the solar radius (0.0047 AU). We note that one would not expect large rocky bodies to be found inside r_{Roche} , so it is unphysical to include such bodies in our initial conditions but doing so is useful to verify our analytic results. Initial eccentricities and inclinations were drawn from a Rayleigh distribution, $f(x) = x/\sigma^2 \exp[-x^2/(2\sigma^2)]$, with $\sigma = 0.01$ for eccentricity and $\sigma = 0^\circ.5$ for inclination. The initial arguments of periapsis, ascending nodes, and mean anomalies were chosen at random from uniform distributions in the interval $[0, 2\pi)$.

As described in Section 3.1, the MFM sets a floor to the size of fragments in our simulations. To investigate how the choice of MFM affects our results, we employed three different MFMs, which are 5, 7.5, and 15 times smaller than the initial masses of the bodies used in our fiducial simulations, or, respectively, 4.0×10^{-3} , $\sim 2.67 \times 10^{-3}$, and $\sim 1.33 \times 10^{-3} M_{\oplus}$. At the density used in this work (3 g cm^{-3}), these bodies have radii of ~ 1200 , ~ 1100 , and ~ 900 km. We ran five simulations for each combination of initial conditions and MFM. A smaller MFM means that more fragments, on average, are produced per collision. Since the time required to calculate gravitational forces goes as the square of the number of bodies, increasing the number of fragments by decreasing the MFM significantly slows down the calculation. This slowdown is exacerbated by the accumulation of fragments inside r_{Roche} , which are unable to merge and thus persist for the duration of the simulation. Therefore the choice for the smallest MFM was limited by computation time. The simulations were run for 3×10^5 years with the exception of the runs with the smallest MFM, $\sim 1.33 \times 10^{-3} M_{\oplus}$, which lasted for only 1×10^5 years, due to limits on computation time.

We adopted a naming convention to organize our numerical results. A name defines a “set of simulations”, by which we mean simulations that have identical initial conditions and MFM but use different seed values for the random number generator. The initial orbital parameters that are chosen at random are eccentricity, inclination, argument of periapsis, ascending node, and mean anomaly. Thus, simulations in a set share identical initial body masses, numbers of bodies, semi-major axes, and MFM. Our three fiducial sets of simulations are described above. The fiducial set with MFM $= 4.0 \times 10^{-3} M_{\oplus}$ is named **fiducial_MFMlarge**, the fiducial set with MFM $\simeq 2.67 \times 10^{-3} M_{\oplus}$ is named **fiducial_MFMmid**, and

TABLE 1
NAMING CONVENTION FOR SIMULATIONS

prefix	description
fiducial	The fiducial set of runs: $150 \times 0.02\text{-}M_{\oplus}$ bodies
numdown	Initial number of bodies half that of the fiducial runs: $75 \times 0.02\text{-}M_{\oplus}$ bodies
numup	Initial number of bodies twice that of the fiducial runs: $300 \times 0.02\text{-}M_{\oplus}$ bodies
massdown	Initial body mass half that of the fiducial runs: $150 \times 0.01\text{-}M_{\oplus}$ bodies
massup	Initial body mass twice that of the fiducial runs: $150 \times 0.04\text{-}M_{\oplus}$ bodies
notidal	Same as the fiducial set of runs, but with tidal effects ignored
merge	Same as the fiducial set of runs, but all collisions assumed to be mergers

the fiducial set with MFM $\simeq 1.33 \times 10^{-3} M_{\oplus}$ is named **fiducial_MFMsmall**. Each set in this work consists of five individual simulations.

To understand how changes to the initial number of bodies affect the outcomes, we ran three sets of simulations with initial conditions and MFM that matched the three fiducial sets except that the initial number of bodies was 75 (instead of 150), as well as three sets of simulations matching the fiducial sets except with 300 initial bodies. The sets with 75 initial bodies have names prepended **numdown** and the sets with 300 initial bodies have names prepended **numup**.

To understand how changes to the total mass present in the initial bodies affected the outcomes, we ran three sets of simulations with initial conditions and MFM that matched the three fiducial sets except that the initial body masses were $0.01 M_{\oplus}$ (instead of $0.02 M_{\oplus}$), as well as three sets of simulations matching the fiducial sets except with initial body masses of $0.04 M_{\oplus}$. The sets with $0.01\text{-}M_{\oplus}$ initial bodies have names prepended **massdown** and the sets with $0.04\text{-}M_{\oplus}$ initial bodies have names prepended **massup**.

We also ran a few sets of control simulations. Three sets had identical initial conditions and MFM as the fiducial sets but the effects of stellar tides were ignored, i.e., the collision algorithm of C13 was followed exactly and Equations (33) and (34) were ignored (i.e., v_e and Q^* were used instead of v'_e and Q^*_{tidal}). These sets have names prepended **notidal**. A fourth set of control simulations had perfect mergers for all collisions, i.e., all collisions were perfectly inelastic and no fragmentation occurred. The name of this set is prepended **merge**.

Table 1 summarizes the prefixes used in our naming scheme for the sets of simulations.

We found that $\sim 10\%$ of the runs failed to finish. An investigation showed that these runs were effectively frozen immediately after collisions that produced $\gtrsim 90$ fragments. We believe that the large number of bodies produced in close proximity to each other after these particularly fragmenting collisions have caused these runs to get bogged down in the Bulirsch-Stoer portion of the hybrid-symplectic integration of *Mercury*. We neglect these failed-to-complete runs in our analysis, but believe that doing so should not bias our conclusions since the results do not appear to depend on the details of the

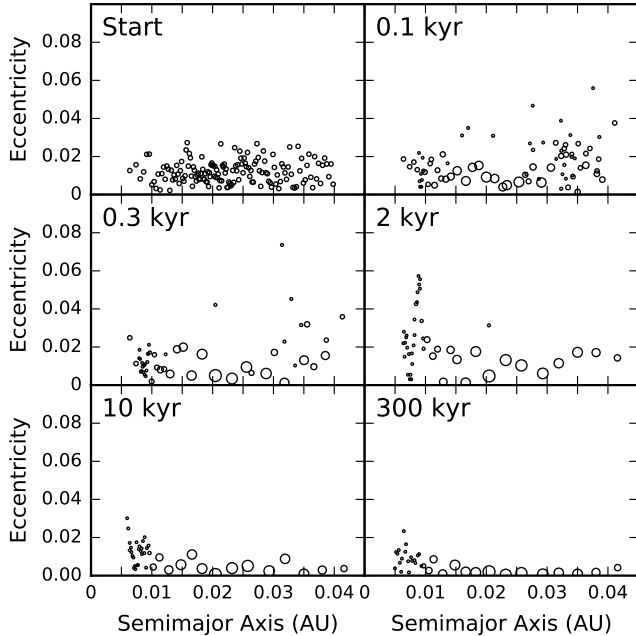


FIG. 1.— Eccentricity versus semi-major axis of all the bodies for one of the `fiducial_MFmlarge` simulations, taken at six different snapshots. The symbol radius is proportional to the radius of each body. The minimum fragment mass (MFM) is $4.0 \times 10^{-3} M_{\oplus}$, the largest value used in this work. At the end of the run, after 3×10^5 years, the system contains 16 bodies on low-eccentricity orbits outside $r_{\text{Roche}} = 0.0089$ AU and 18 fragments inside r_{Roche} .

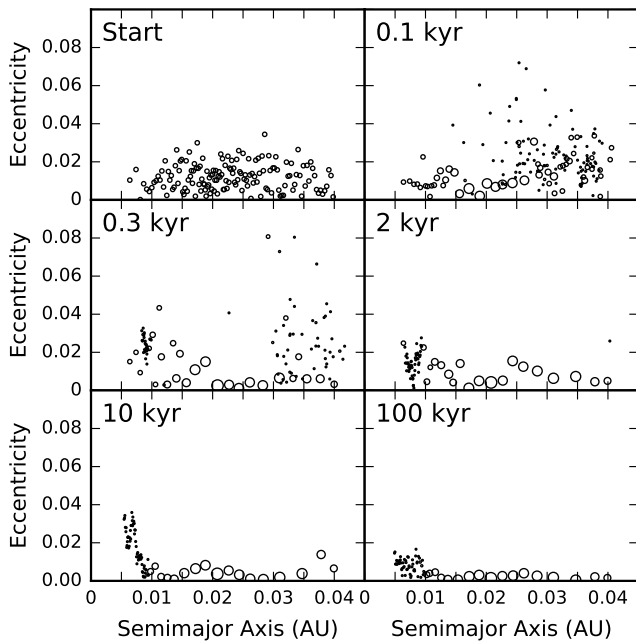


FIG. 2.— Same as Figure 1, but for one of the `fiducial_MFMsmall` simulations, with MFM set to $\sim 1.33 \times 10^{-3} M_{\oplus}$, a factor of three smaller than in Figure 1. Note that the final snapshot is at 100 kyr instead of 300 kyr as in Figure 1; this simulation was not run as long due to the larger computational demands of runs with smaller MFM. At the end of the run, the system contains 24 bodies on low-eccentricity orbits outside r_{Roche} (several of which are fragments inside $1.1 r_{\text{Roche}}$) and 45 fragments inside r_{Roche} .

collision history during the run. We also ran supplementary simulations, of which a sufficient number completed to make up for the runs that failed to complete. For supplementary `numup` and `massup` runs, it was necessary to set a maximum number of fragments that could be produced in a single collision to allow any of the runs to successfully complete. The maximum number of fragments used for these runs was 50.

4. RESULTS

We present the results from our fiducial runs in Section 4.1 and then describe the results from our variations on the fiducial runs in Section 4.2.

4.1. Fiducial runs

Figure 1 shows several snapshots of eccentricity vs. semi-major axis from one of the `fiducial_MFmlarge` simulations. Within 100 years, several of the bodies have already built up to large fractions of their final masses. This may seem fast, but by 100 years bodies with $a = 0.01$ AU have gone through 10^5 orbits. Over the remainder of the simulation, the planets continue building up to their final masses by accumulating the remaining smaller bodies and merging with each other. The fragments inside (and just outside) the Roche radius never consolidate, as expected from the collision algorithm, and end up with larger (but still small) eccentricities at the end of the simulation than the planets outside r_{Roche} . Figure 2 is the same as Figure 1 but for one of the `fiducial_MFMsmall` simulations, which has an MFM that is three times smaller than the run shown in Figure 1. Other than a larger buildup of fragments inside r_{Roche} and an increased number of fragments outside r_{Roche} in the intermediate stages, the simulation proceeds qualitatively the same as that in Figure 1. In both runs, the fragments are unable to accumulate for $a \lesssim 0.01$ AU, which is $\sim 10\%$ larger than r_{Roche} . This behavior occurs in all `fiducial_MFmlarge`, `fiducial_MFMmid`, and `fiducial_MFMsmall` runs. The lack of planet formation between r_{Roche} and $\sim 1.1 r_{\text{Roche}}$ is presumably due to the large tidal forces acting on the bodies in that regime, which enhance the amount of fragmentation that occurs and makes it more difficult for bodies to merge, especially for collisions between bodies of similar size ($\alpha \approx 1$). This behavior has been studied in detail in the context of ring particles by, e.g., Canup & Esposito (1995) and Yasui et al. (2014). Our control runs (`merge` and `notidal`), which ignore tidal effects, form planets at all semi-major axes that were populated in the initial state, even well inside r_{Roche} .

The eccentricities of the planets in Figure 1 get damped over time, and the final mean eccentricity of the 16 bodies outside r_{Roche} is only 0.0028. To determine the source of the eccentricity damping, we re-ran some of the fiducial runs with a single modification: at 1.5×10^4 years, all bodies inside a radius r_{clear} were removed. We experimented with $r_{\text{clear}} = r_{\text{Roche}}$ and $r_{\text{clear}} = 1.1 r_{\text{Roche}}$. Eccentricity damping still occurred in the simulations of the $r_{\text{clear}} = r_{\text{Roche}}$ sets but the eccentricity damping in the $r_{\text{clear}} = 1.1 r_{\text{Roche}}$ sets ceased at the time of body removal. Thus, the eccentricity damping seems to be due mainly to the bodies between r_{Roche} and $1.1 r_{\text{Roche}}$.

Figure 3 shows the number of bodies as a function of time for all the simulations in the `fiducial_MFmlarge`,

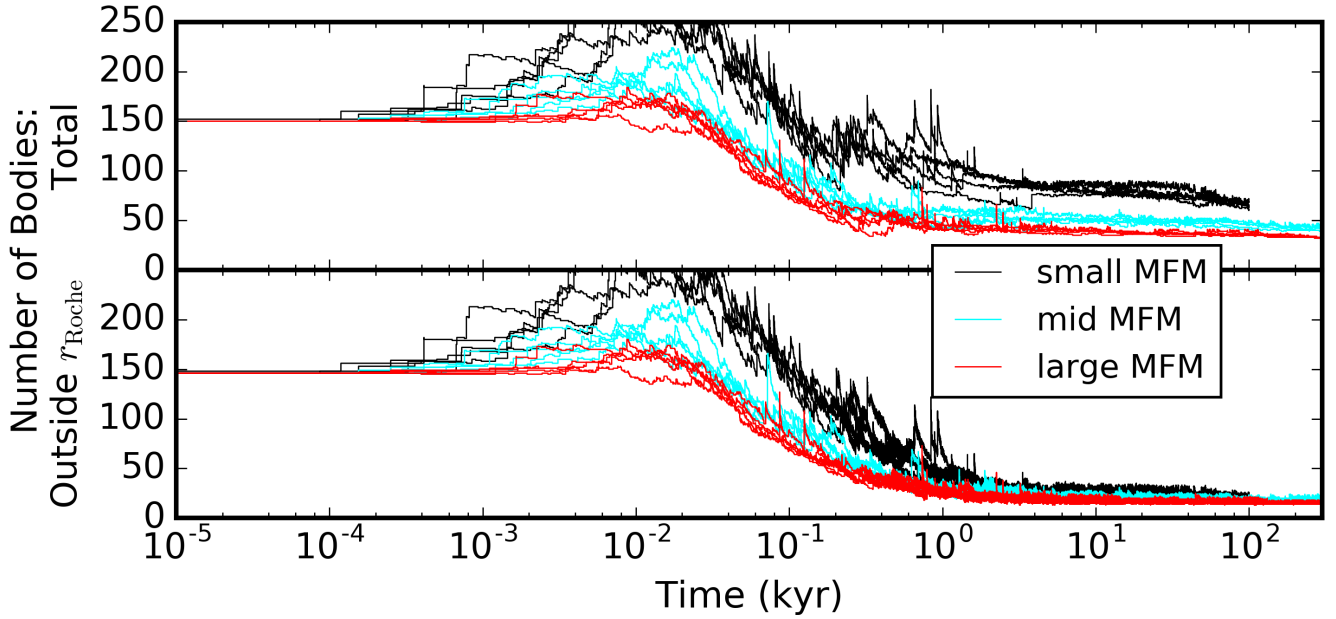


FIG. 3.— The number of bodies as a function of time for the five simulations in each of the three fiducial sets. The top panel shows the total number of bodies, while the bottom panel shows only those bodies that are outside r_{Roche} . The simulations from each set are encoded by color: “large MFM” corresponds to `fiducial_MFMlarge` ($\text{MFM} = 1.2 \times 10^{-8} M_{\odot}$) and is shown in red, “mid MFM” corresponds to `fiducial_MFMmid` ($\text{MFM} = 0.8 \times 10^{-8} M_{\odot}$) and is shown in cyan, and “small MFM” corresponds to `fiducial_MFMsmall` ($\text{MFM} = 0.4 \times 10^{-8} M_{\odot}$) and is shown in black. All simulations converge on a final set of planets outside r_{Roche} with similar properties ($N \simeq 15$, $\langle e \rangle \simeq 0.003$).

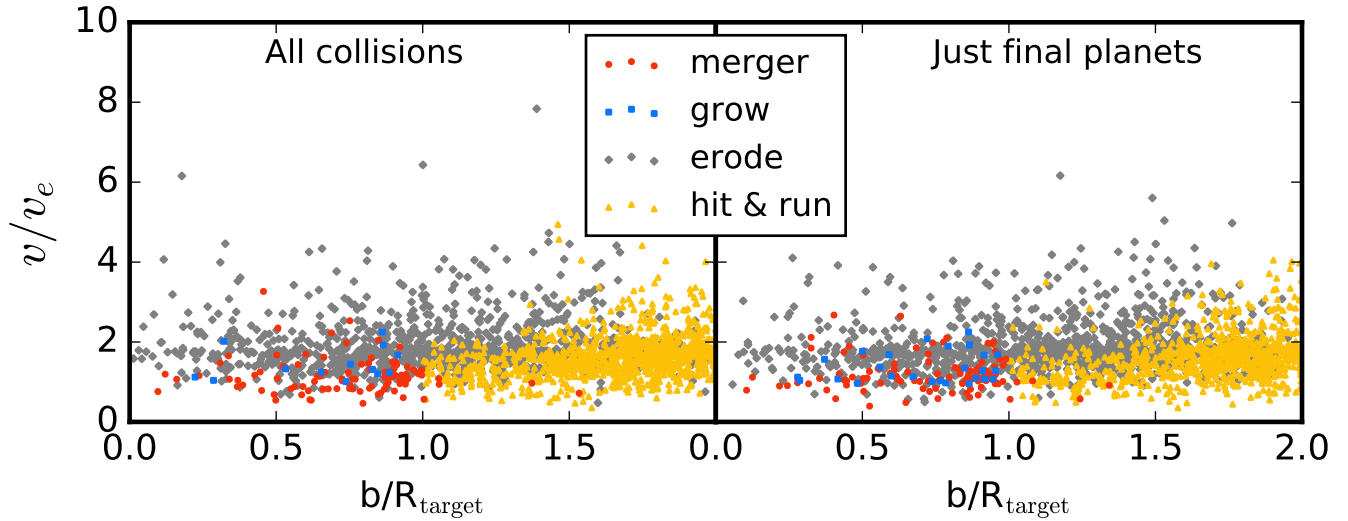


FIG. 4.— A random sample of collision outcomes for the same `fiducial_MFMlarge` simulation shown in Figure 1. The plots show impact velocity versus impact parameter for collisions occurring outside r_{Roche} . The impact parameter b is defined as the distance between the centers of the two bodies at the time of the collision, projected perpendicular to the relative velocity vector. Only a random sample of 2000 collision outcomes is shown in each panel to prevent overcrowding. The left panel shows a random sampling of all collisions (total number: 88,659) and the right panel shows a sampling of the collisions involving the bodies that become the final planets (total number: 4,625). In the legend, “merger” refers to collisions that were treated in the code as mergers or as graze-and-merge collisions, “hit & run” refers to collisions classified as hit-and-run (high impact parameter, no mass loss for target body), while among non-hit-and-run fragmenting collisions those with the largest body losing mass in the collision are labeled as “erode” and those with the largest body coming out of the collision with at least as much mass as before the collision are labeled as “grow”. The division at $b/R_{\text{target}} = 1$ between “grow” collisions and “hit & run” collisions is due to the definition of hit-and-run collisions, as detailed in LS12 and C13. There are far more erosive and hit-and-run collisions than collisions that lead to mass growth; however, a closer look reveals that most these are within $\sim 1.1 r_{\text{Roche}}$. See text for details.

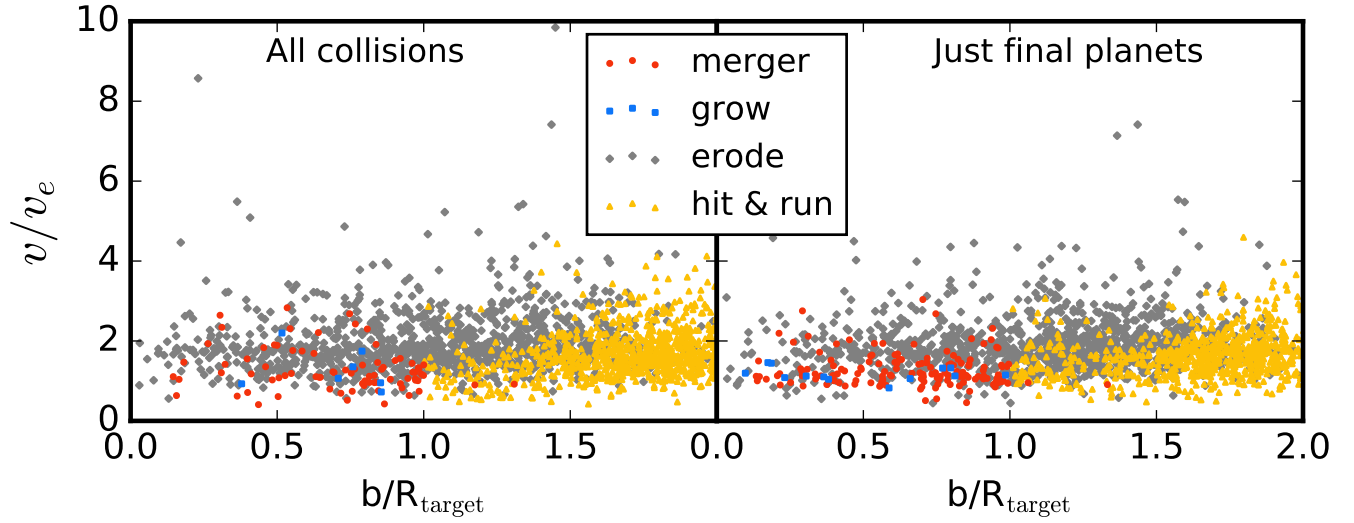


FIG. 5.— Same as Figure 4, but for a simulation from the `fiducial_MFMsmall` set (the same simulation as shown in Figure 2). The total number of collisions is 344,847 and the total number of collisions involving the bodies that become the final planets is 10,003.

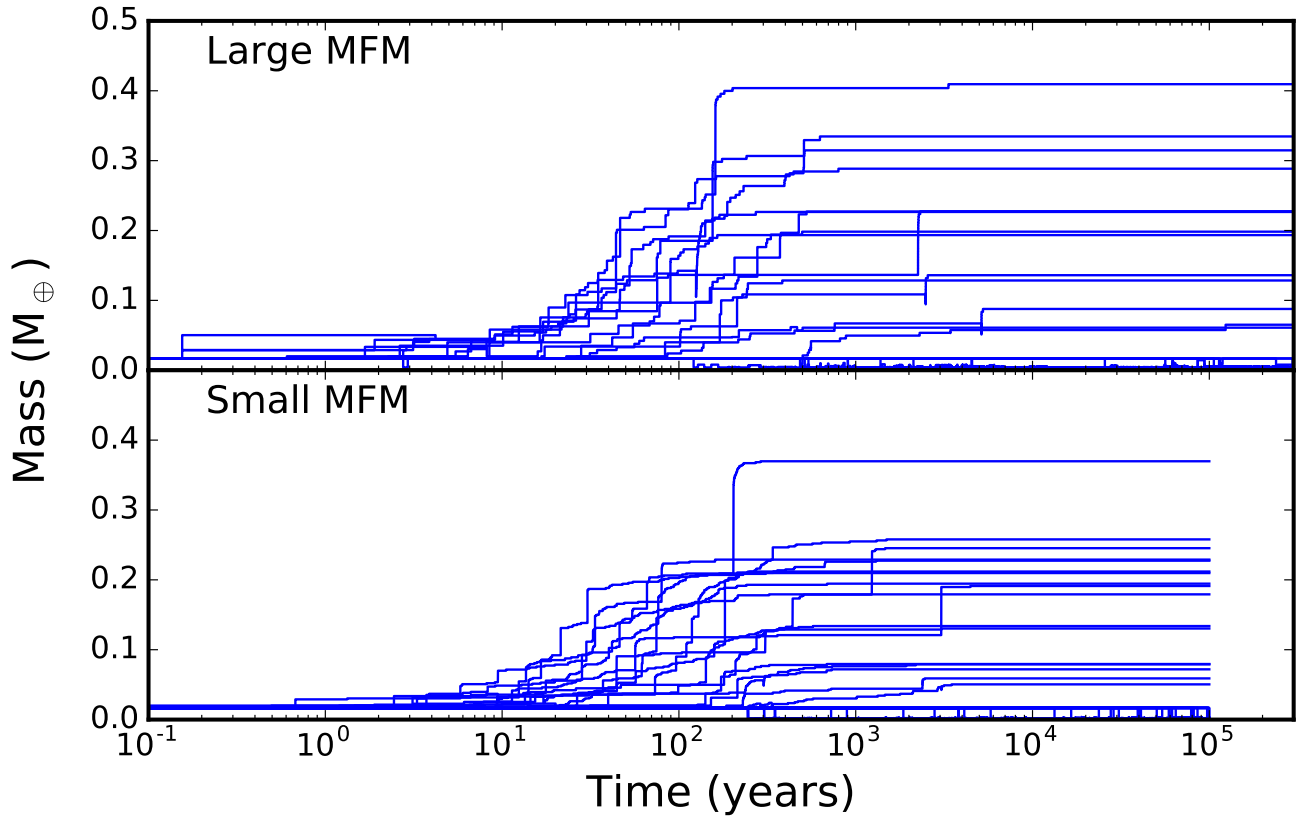


FIG. 6.— Mass as a function of time for bodies that become the final planets. The top panel shows one of the simulations from the `fiducial_MFMlarge` set (the same simulation as in Figures 1 and 4) while the bottom panel shows one of the simulations from the `fiducial_MFMsmall` set (the same simulation as in Figures 2 and 5). The final planets outside $1.1 r_{\text{Roche}}$ exhibit a steady march to their final masses, with relatively few erosive collisions. Note that the simulations of the bottom panel were run for less time than those of the top panel, as described in Section 3.2.

`fiducial_MFMmid`, and `fiducial_MFMsmall` sets. The top panel shows the total number of bodies while the bottom panel shows only those bodies outside r_{Roche} . In the latter case, the number of bodies converges to a constant value of ~ 15 bodies outside r_{Roche} by ~ 100 kyr, independent of MFM. In what follows, we regard the bodies present outside r_{Roche} at the end of the integrations as the “final planets” (even though those inside $\sim 1.1 r_{\text{Roche}}$ have not built up to typical planetary masses), while the bodies present inside r_{Roche} at the end of the integrations are referred to as “fragments”, because these bodies have fragmented down to nearly the MFM. The number of fragments has also converged to a constant value in each run, as can be seen in the top panel of Figure 3.

In both panels of Figure 3, the number of bodies shows a persistent trend downward with time in each simulation after the first 30 years or so. The downward trend is interrupted occasionally by collisions that produce a large number of fragments, especially for lower-MFM runs. However, these fragments get quickly reaccumulated and there is never any runaway fragmentation. In all of our simulations, a system of 14–24 planets is always formed outside r_{Roche} (with 11–17 bodies outside $1.1 r_{\text{Roche}}$).

The left panel of Figure 4 shows a sample of the collision outcomes in one of the `fiducial_MFMLarge` simulations and the right panel shows a sample of the subset of collision outcomes involving the bodies that become the final planets. Figure 5 shows the same for one of the `fiducial_MFMsmall` runs. In these figures, and in the discussion that follows, only collisions that occurred outside r_{Roche} are considered. The collisions are classified into one of four categories: “merger”, “grow”, “erode”, and “hit & run”. Collisions that were treated in the code as mergers or as graze-and-merge collisions are here collectively classified as “merger”, hit-and-run collisions are classified as “hit & run”, while among non-hit-and-run fragmenting collisions those where the largest body loses mass are classified as “erode” and those where the largest body comes out of the collision with at least as much mass as before are classified as “grow”. In the right panel of Figure 4, 6% of collisions were classified as “merger” and 1% were classified as “grow”, compared to 5% and 0.9% for all collisions. These percentages are characteristic of all of the `fiducial_MFMLarge` runs. Remarkably, the bodies that became the final planets had a larger percentage of “erode” collisions than did all the bodies: 52% for the run in Figure 4 for the final planets as compared with 46% among all the collisions. For all five `fiducial_MFMLarge` runs, the percentage of “erode” collisions was higher among the bodies that became the final planets than among all the bodies. Similar patterns were found among the `fiducial_MFMsmall` runs, one of which is shown in Figure 5: all five of the runs had a greater fraction of “merger” and “grow” collisions among collisions involving just the bodies that became the final planets than all the bodies, and four of the five runs had a greater fraction of “erode” collisions among collisions involving just the bodies that became the final planets than all the bodies. For the run shown in Figure 5, 7% of collisions involving bodies that became the final planets were “merger”, 0.7% were “grow”, and 55% were “erode”, as compared to 4% “merger”, 0.3% “grow”, and 54% “erode” collisions among all the bodies.

For all ten of the runs in the `fiducial_MFMLarge` and `fiducial_MFMsmall` sets, the fraction of “hit & run” collisions is lower among collisions involving just the bodies that became the final planets than among all the bodies.

It may seem strange that the collisions involving just the bodies that became the final planets had a larger fraction of “erode” collisions than for all the bodies, since those bodies were able to gain sufficient mass to become planets by the end of the simulations. However, most of these erosive collisions occurred close to r_{Roche} , while further out from r_{Roche} a larger fraction of collisions lead to mass growth. Close to r_{Roche} , tidal effects cause a larger fraction of the collisions to be fragmenting. Specifically, for the bodies that became the final planets of the `fiducial_MFMLarge` run shown in Figure 4, 99.5% of “erode” collisions occurred inside 0.01 AU ($\sim 1.13 r_{\text{Roche}}$) as well as 86% of hit & run collisions, while only 8.8% of “merger” and 3.4% of “grow” collisions occurred inside 0.01 AU. Thus, the vast majority of erosive collisions occur close to r_{Roche} , where tides are the strongest, and the majority of collisions leading to mass growth occur outside 0.01 AU, where the final planetary system forms. Comparable numbers are found for all runs in the `fiducial_MFMLarge`, `fiducial_MFMmid`, and `fiducial_MFMsmall` sets. In short, the bodies outside $\sim 1.1 r_{\text{Roche}}$ that become the final planets mostly engage in collisions that lead to mass growth, while most of the fragmenting collisions occur inside $\sim 1.1 r_{\text{Roche}}$, where tidally enhanced fragmentation prevents a steady accumulation of mass.

Figure 6 shows the masses of the bodies that become the final planets as a function of time. In this work and for this figure, the largest remnant in a collision adopts the name of the more massive of the two impacting bodies. The final planets outside $1.1 r_{\text{Roche}}$ have masses between ~ 0.05 and $\sim 0.4 M_{\oplus}$. Each vertical “jump” in mass represents a collision. The bodies that undergo significant mass growth (i.e., the final planets outside of $\sim 1.1 r_{\text{Roche}}$) have nearly uninterrupted marches towards higher masses. We must keep in mind, though, that the bodies in Figure 6, by virtue of their growth and their surviving to the end, exhibit a selection bias in which kinds of collisions they experienced. The planets assemble very quickly, with most reaching their final masses within $\sim 10^3$ years.

Figure 7 shows the separation between adjacent bodies at the end of the simulations in units of r_{Hill} . Here, separation is defined as the difference of the apastron of the inner body and the periastron of the outer body. The condition for long-term stability (over 10^{10} orbits, or 10 million years at 0.01 AU) of a final planetary configuration is that the separations exceed $\sim 10 r_{\text{Hill}}$ (Pu & Wu 2015). For bodies outside r_{Roche} (denoted with the vertical dashed line), this condition is met, with only a small fraction of the bodies having separation $< 10 r_{\text{Hill}}$. This result confirms our use of $f_3 = 10$ in Section 2. Inside r_{Roche} , the fragments show a large spread in separations and the separations are, on average, smaller than those of the planets outside r_{Roche} . In particular, separations as small as $r_{\text{Hill}} \approx 0$ are seen. The small values of these separations are partly due to the relatively high eccentricities (see Figures 1 and 2) and partly due to the inability of the bodies inside r_{Roche} to merge and evolve

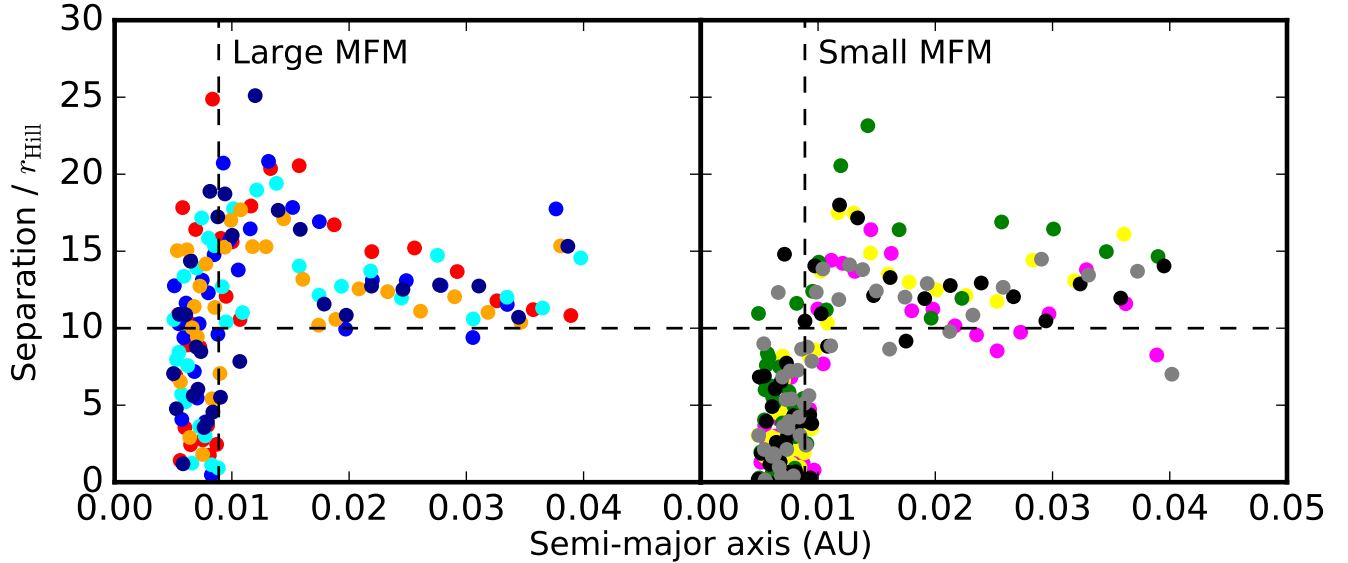


FIG. 7.— The separation between adjacent bodies (defined as the difference between apastron of the inner body and periastron of the outer body) in units of r_{Hill} as a function of semi-major axis at the end of the simulation. Here, the semi-major axis is calculated as the mean of the apastron of the inner body and the periastron of the outer body. Each color corresponds to bodies from a single simulation. The vertical dashed line shows the location of r_{Roche} . The left panel shows results from the `fiducial_MFMlarge` simulations while the right panel shows results from the `fiducial_MFMsmall` simulations. The minimum separation required for stability over 10^{10} orbits (10 million years at 0.01 AU) is $\sim 10 r_{\text{Hill}}$ (Pu & Wu 2015), marked by a horizontal dashed line. The separations of bodies inside r_{Roche} are smaller, partly because the eccentricities are higher and partly because we do not allow these bodies to merge to form more stable systems.

into a dynamically stable system.

Figure 8 shows the final planetary configurations for our fiducial runs. The semi-major axes of the planets with the most mass in each system are clustered around ~ 0.2 – 0.3 AU. As was noted earlier, tidally enhanced fragmentation prevents planet formation out to ~ 0.01 AU, which is $\sim 1.1 r_{\text{Roche}}$. All of the fiducial runs form a final, stable planetary system. The planet-formation efficiency (the fraction of mass initially present that is incorporated into the final planets) for the mass initially outside $\sim 1.1 r_{\text{Roche}}$ is $\sim 100\%$, while inside it is much lower because the tidally enhanced fragmentation prevents planets from growing, decreasing with radius to be approximately zero near r_{Roche} . The high planet-formation efficiency outside $\sim 1.1 r_{\text{Roche}}$ is partly an artifact of the MFM, which prevents mass loss through collisional cascades.

4.2. Other scenarios

Our other sets of runs with tidal effects (`numdown`, `numup`, `massdown`, `massup`; see Table 1) also formed planets all the way down to $\sim 1.1 r_{\text{Roche}}$. The distribution and masses of the planets in the final systems of these sets differed from our fiducial sets in ways that related to the differing initial conditions: runs with a larger total initial mass (`numup` and `massup`) produced a smaller number (~ 10) of higher-mass planets in their final systems than did the fiducial sets, while the runs with a smaller total initial mass (`numdown` and `massdown`) produced about the same number of planets in their final systems as our fiducial sets, but with lower masses. As mentioned previously, our control runs (`notidal` and `merge`) also form planets and are able to do so at semi-major axes as small as $\sim 0.6 r_{\text{Roche}}$ (planet formation at smaller semi-major axes is suppressed only because our initial conditions do not have mass interior to 0.005 AU). The details of how the various runs got to their final configurations also

differed from the fiducial sets; for instance, more fragmentation occurred in the `numup` runs than in the fiducial set—likely due to the increased mass available to be turned into fragments—and the numbers of bodies in the `numup_MFMsmall` runs was as high as ~ 700 before accumulation was able to take over and reduce the total number of bodies. The planet formation efficiency for these runs for the mass initially outside $\sim 1.1 r_{\text{Roche}}$ is also $\sim 100\%$, as it was for the fiducial runs. Figure 9 shows the final configurations of a random selection of the `numdown`, `numup`, `massdown`, `massup`, `notidal`, and `merge` runs.

5. DISCUSSION

The analytic work of Section 2 concluded that collisional fragmentation was not a barrier to planet formation outside of the Roche radius. Our numerical integrations, described in Sections 3 and 4, enhanced our analytic work by including the effects of stellar tides and off-center collisions. Even with the richer physics, the results of our numerical integrations agree with the analytic arguments, except for a small region between r_{Roche} and $\sim 1.1 r_{\text{Roche}}$, where stellar tides are strong enough that even relatively weak collisions lead to fragmentation.

Other works have examined *in situ* formation of rocky planets at small semi-major axes (Hansen & Murray 2012; Ogihara et al. 2015; Dawson et al. 2016; Moriarty & Ballard 2016; Matsumoto & Kokubo 2017). However, these investigations (i) did not consider collisional fragmentation; (ii) examined only initial semi-major axes larger than 0.04 AU, whereas we focused on smaller semi-major axes. Our fiducial simulations start with $3M_{\oplus}$ of solid material, about three times larger than the mass expected in the minimum-mass solar nebula between 0.01 AU and 0.04 AU (Weidenschilling 1977; Hayashi 1981),

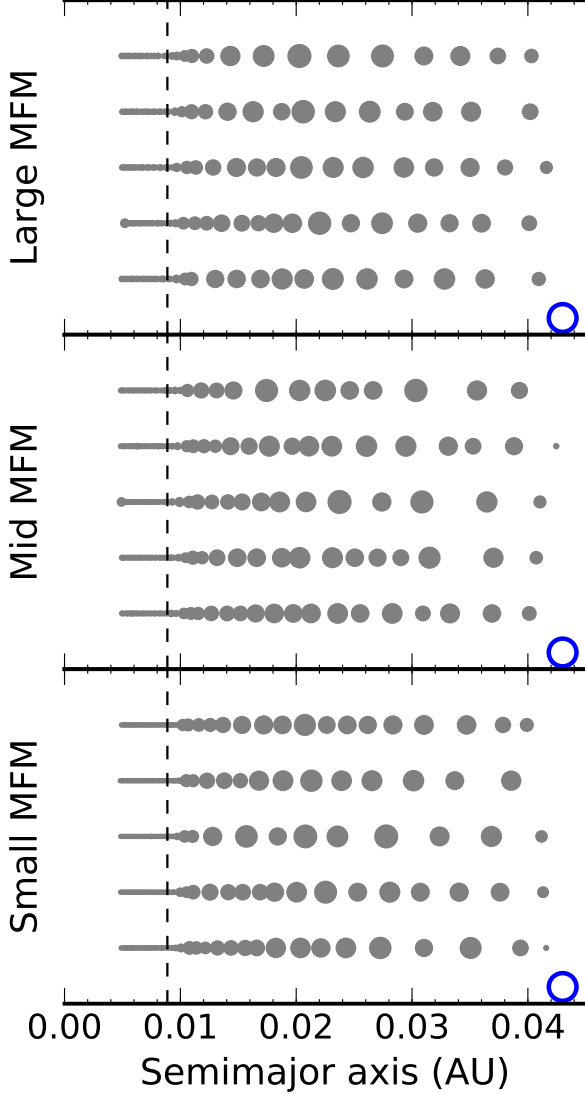


FIG. 8.— The final planetary configurations for all the fiducial sets of simulations. The top panel shows final configurations from the `fiducial_MFMlarge` set, the middle panel shows final configurations from the `fiducial_MFMmid` set, and the bottom panel shows final configurations for simulations from the `fiducial_MFMsmall` set. Each row of circles corresponds to the final bodies of a single simulation. The radius of each circle is scaled by the final radius of the corresponding body, assuming the same density for all bodies. The blue circle in the bottom right of each panel shows the radius of a $1\text{-}M_{\oplus}$ body at this density. The vertical dashed line shows the location of r_{Roche} . All of our fiducial simulations form a stable planetary system at all orbital radii greater than $\sim 1.1 r_{\text{Roche}}$. The gray horizontal line to the left of ~ 0.01 AU is a series of overlapping circles representing the closely spaced fragments found at these semi-major axes.

which is comparable to the disk profiles used by the referenced authors (of course, the applicability of the minimum-mass solar nebula to these small radii is highly uncertain). Their simulations typically ran for $\sim 1\text{--}10$ Myr. Our simulations ran for only 0.3 Myr because the dynamical time at these small radii is much shorter; the shorter integrations are justified because the numbers and properties of the planets seemed to be stable well before the end of the integration (see Figure 6).

Not considered in this work is the potential loss of

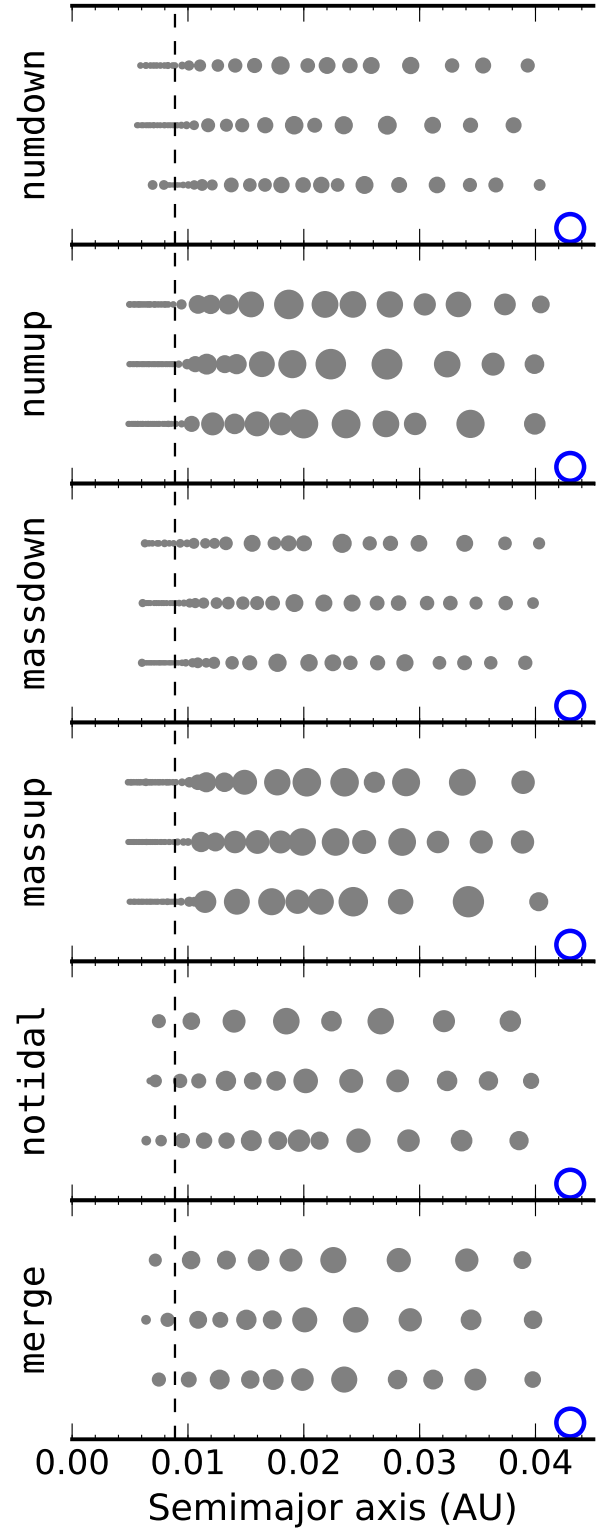


FIG. 9.— Same as Figure 8 but for final planetary systems from our initial setups other than `fiducial`.

mass due to Poynting–Robertson (PR) drag on dust and small pebbles produced in collisional cascades. Bodies of 1-cm radius with density of 1 g cm^{-3} around solar-type stars have PR drag lifetimes of ~ 10 kyr at 0.04 AU and ~ 1 kyr at 0.01 AU, with smaller bodies having shorter lifetimes proportional to their radius (e.g., Wyatt & Whipple 1950). If a sufficient number of other small bodies are present, lifetimes due to collisional cascades can be even less than PR lifetimes (e.g., Wyatt 2008). Depending on the amount of small bodies produced in fragmenting collisions, these processes may lead to significant mass loss, especially near r_{Roche} due to the enhanced fragmentation that occurs there.

Also not considered in this work is the effect of large planets on wider orbits on the formation and evolution of inner planetary systems. A sufficiently close and massive gas giant could stir up the bodies and produce larger eccentricities and higher collision velocities while the planets are forming. The potential effects of gas giants depend on the relative times at which they form; the giant planets would need to be in place before inner planet formation has ceased in order to have an effect. Stirring from giant planets would also increase the separation necessary between bodies for long-term stability.

This work assumes no tidal damping of eccentricity or semi-major axis. This assumption is justified based on calculations of the tidal damping timescales (e.g., Jackson et al. 2008). For these calculations, we assumed a Sun-like star, a $0.5\text{-}M_{\oplus}$ planet with $a = 0.01$ AU, and $Q_{\text{star}} = 10^{5.5}$ and $Q_{\text{planet}} = 100$ for the tidal dissipation parameters of the star and planet. For these values, the eccentricity damping timescale is $\sim 10^5$ yr and the semi-major axis damping timescale is $\sim 10^{10}$ yr, compared to the ~ 100 – 1000 year timescale for planets to form in our simulations and the 3×10^5 year length of our longest simulations. So, although eccentricity damping is negligible on the timescales of planet formation, it could affect the longer-term evolution and cleanup of the system. Since eccentricity damping leads to lower-velocity collisions on average, it should not modify the main conclusion of this work, that planet formation is not suppressed by fragmentation.

This work also assumes there is no gas left in the disk at the later stages of planet formation examined here. With the short ~ 100 year formation timescale found in our simulations starting from lunar-sized bodies, though, this assumption may be incorrect. This, of course, depends on the gas dissipation timescale at small radii, which is highly uncertain.

Future work could improve on the collision algorithm of C13 by implementing a size distribution for the fragments resulting from a collision, as was done by LS12. This would lead to a richer variety of mass ratios in collisions than were present in this work. Additionally, our initial conditions assumed that all the bodies started out with the same mass. A more detailed follow-up could look at a more realistic size distribution for the initial bodies, as well as taking into account the continued formation of large bodies from accumulating planetesimals (similar to McNeil et al. 2005), which would also lead to

a richer distribution in mass ratios. Since, as was shown in Section 2.3, collisional growth is robust across all mass ratios, we do not expect that a more realistic size distribution of collision fragments or initial bodies will affect our main conclusions.

As was pointed out in Section 2, differentiated bodies behave differently in collisions than homogeneous bodies, and bodies of the masses encountered in this work (\gtrsim lunar mass) are likely to have significant differentiation. Head-on collisions of differentiated bodies have higher values of f_2 relative to homogeneous bodies and thus require higher-velocity collisions to lead to fragmentation, while off-center collisions have lower values of f_2 (Asphaug 2010), so these two effects will partially cancel each other. Even if the off-center collisions with a lower f_2 dominate, the analytic calculation and arguments of Section 2.3 give $a_{\text{frag}} \approx 1.1 r_{\text{Roche}}$ as likely for equal-mass bodies; thus, differentiation of bodies is not expected to modify our conclusions significantly. A collision prescription that combines the general applicability and scaling laws of LS12 with results of collisions between differentiated bodies similar to Asphaug (2010) would allow for simulating systems of differentiated bodies in similar style as this work.

6. CONCLUSION

We have carried out both analytic and numerical investigations of collisional rocky planet formation at small semi-major axes (~ 0.01 AU) to determine whether collisional fragmentation is a barrier to planet formation. Our analytic argument (which ignores tidal effects) predicts that collisions leading primarily to mass growth are possible all the way down to the Roche radius and, thus, collisional fragmentation is not a barrier to planet formation. Our numerical integrations (which include tidal effects), starting with \sim lunar-sized bodies, are able to form planets all the way down to $a \simeq 1.1 r_{\text{Roche}}$. Control integrations that ignore the effects of tides are able to form planets at even smaller semi-major axes, consistent with our analytic result. Our numerical results thus confirm that collisional fragmentation is not a barrier to rocky planet formation, except perhaps in a narrow range of distances within 10% of r_{Roche} . The resulting planetary systems are expected to be stable over long time scales ($\sim 10^{10}$ orbits).

We thank Bill Bottke, Eve Lee, and Hilke Schlichting for illuminating conversations. We also thank the referee for a thorough reading of the manuscript and many constructive comments. This research has made use of NASA’s Astrophysics Data System Bibliographic Services, the Exoplanet Orbit Database and the Exoplanet Data Explorer at exoplanets.org (Han et al. 2014), and the NASA Exoplanet Archive, which is operated by the California Institute of Technology, under contract with the National Aeronautics and Space Administration under the Exoplanet Exploration Program. The figures in this work were made using the Matplotlib module for Python (Hunter 2007).

REFERENCES

- Asphaug, E. 2010, *Chemie der Erde / Geochemistry*, 70, 199
- Baraffe, I., Homeier, D., Allard, F., & Chabrier, G. 2015, *A&A*, 577, A42

- Baruteau, C., Crida, A., Paardekooper, S.-J., et al. 2014, in *Protostars and Planets VI*, ed. H. Beuther, R. S. Klessen, C. P. Dullemond, & T. Henning (Tucson: University of Arizona Press), 667
- Benz, W., Ida, S., Alibert, Y., Lin, D., & Mordasini, C. 2014, in *Protostars and Planets VI*, ed. H. Beuther, R. S. Klessen, C. P. Dullemond, & T. Henning (Tucson: University of Arizona Press), 691
- Canup, R. M., & Esposito, L. W. 1995, *Icarus*, 113, 331
- Chambers, J. E. 1999, *MNRAS*, 304, 793
- . 2001, *Icarus*, 152, 205
- . 2013, *Icarus*, 224, 43
- Charbonneau, D., Berta, Z. K., Irwin, J., et al. 2009, *Nature*, 462, 891
- Chatterjee, S., & Tan, J. C. 2014, *ApJ*, 780, 53
- . 2015, *ApJ*, 798, L32
- Chiang, E., & Youdin, A. N. 2010, *Annual Review of Earth and Planetary Sciences*, 38, 493
- D'Alessio, P., Cantö, J., Calvet, N., & Lizano, S. 1998, *ApJ*, 500, 411
- Dawson, R. I., Lee, E. J., & Chiang, E. 2016, *ApJ*, 822, 54
- Dohnanyi, J. S. 1969, *J. Geophys. Res.*, 74, 2531
- Dominik, C., & Decin, G. 2003, *ApJ*, 598, 626
- Genda, H., Kokubo, E., & Ida, S. 2012, *ApJ*, 744, 137
- Gillon, M., Triaud, A. H., Demory, B.-O., et al. 2017, *Nature*, 542, 456
- Han, E., Wang, S. X., Wright, J. T., et al. 2014, *PASP*, 126, 827
- Hansen, B. M. S., & Murray, N. 2012, *ApJ*, 751, 158
- Hayashi, C. 1981, *Progress of Theoretical Physics Supplement*, 70, 35
- Hénon, M., & Petit, J.-M. 1986, *Celestial Mechanics*, 38, 67
- Holsapple, K. A., & Michel, P. 2006, *Icarus*, 183, 331
- . 2008, *Icarus*, 193, 283
- Hunter, J. D. 2007, *Computing In Science & Engineering*, 9, 90
- Hyodo, R., & Ohtsuki, K. 2014, *ApJ*, 787, 56
- Jackson, B., Greenberg, R., & Barnes, R. 2008, *The Astrophysical Journal*, 678, 1396
- Karjalainen, R. 2007, *Icarus*, 189, 523
- Kenyon, S. J., & Bromley, B. C. 2017a, *ApJ*, 844, 116
- . 2017b, *ApJ*, 839, 38
- Kobayashi, H., & Tanaka, H. 2010, *Icarus*, 206, 735
- Leinhardt, Z. M., & Stewart, S. T. 2012, *ApJ*, 745, 79
- Matsumoto, Y., & Kokubo, E. 2017, *AJ*, 154, 27
- McNeil, D., Duncan, M., & Levison, H. F. 2005, *AJ*, 130, 2884
- Moriarty, J., & Ballard, S. 2016, *ApJ*, 832, 34
- Muirhead, P. S., Johnson, J. A., Apps, K., et al. 2012, *ApJ*, 747, 144
- Ogihara, M., Morbidelli, A., & Guillot, T. 2015, *A&A*, 578, A36
- Pan, M., & Sari, R. 2005, *Icarus*, 173, 342
- Pu, B., & Wu, Y. 2015, *ApJ*, 807, 44
- Raymond, S. N., & Cossou, C. 2014, *MNRAS*, 440, L11
- Schlichting, H. E. 2014, *ApJ*, 795, L15
- Stewart, S. T., & Leinhardt, Z. M. 2009, *ApJ*, 691, L133
- . 2012, *ApJ*, 751, 32
- Weidenschilling, S. J. 1977, *Ap&SS*, 51, 153
- Wetherill, G. W., & Stewart, G. R. 1989, *Icarus*, 77, 330
- Wyatt, M. C. 2008, *ARA&A*, 46, 339
- Wyatt, M. C., & Dent, W. R. F. 2002, *MNRAS*, 334, 589
- Wyatt, S. P., & Whipple, F. L. 1950, *ApJ*, 111, 134
- Yasui, Y., Ohtsuki, K., & Daisaka, H. 2014, *ApJ*, 797, 93
- Youdin, A. N., & Chiang, E. I. 2004, *ApJ*, 601, 1109
- Youdin, A. N., & Shu, F. H. 2002, *ApJ*, 580, 494